HOMOGENIZATION TECHNIQUE TO PERFORM PERIODIC UNIT CELL CALCULATIONS USING SPRING ELEMENTS

M.Tech. Thesis

By

DEVESH AGRAWAL

DEPARTMENT OF MECHANICAL ENGINEERING

INDIAN INSTITUTE OF TECHNOLOGY INDORE

JUNE 2025

HOMOGENIZATION TECHNIQUE TO PERFORM PERIODIC UNIT CELL CALCULATIONS USING SPRING ELEMENTS

A THESIS

Submitted in partial fulfillment of the
requirements for the award of the degree
of
Master of Technology

by

DEVESH AGRAWAL

DEPARTMENT OF MECHANICAL ENGINEERING
INDIAN INSTITUTE OF TECHNOLOGY INDORE
JUNE 2025

INDIAN INSTITUTE OF TECHNOLOGY INDORE

CANDIDATE'S DECLARATION

I hereby certify that the work which is being presented in the thesis entitled **HOMOGENIZATION TECHNIQUE TO PERFORM PERIODIC UNIT CELL CALCULATIONS USING SPRING ELEMENTS** in the partial fulfillment of the requirements for the award of the degree of **MASTER OF TECHNOLOGY** and submitted in the **DEPARTMENT OF MECHANICAL ENGINEERING, Indian Institute of Technology Indore**, is an authentic record of my own work carried out during the time period from July 2023 to June 2025 under the supervision of **Dr. Mayank Chouksey**, Assistant Professor, **Indian Institute of Technology Indore.**

The matter presented in this thesis has not been submitted by me for the award of any other degree of this or any other institute.

D Agrawal
14/06/25

DEVESH AGRAWAL
(M.TECH. STUDENT)

This is to certify that the above statement made by the candidate is correct to the best of my/our knowledge.

14/06/2025

DR. MAYANK CHOUKSEY
(THESIS SUPERVISOR)

DEVESH AGRAWAL has successfully given his/her M.Tech. Oral Examination held on **23 MAY 2025**.

Signature(s) of Supervisor(s) of M.Tech. thesis
Date: 14/06/2025

Convener, DPGC
Date:17-06-2025

ACKNOWLEDGEMENTS

I would like to express my sincere gratitude to my thesis supervisor, **Dr. Mayank Chouksey**, for his constant guidance, support, and valuable insights throughout the course of this work. His mentorship has been crucial to the success of this thesis. I also thank **Dr. Indresen Singh** for providing access to lab facilities and a productive research environment.

I'm grateful to my lab mates in the **Computational Solid Mechanics Laboratory** for their help, discussions, and encouragement during this journey. I also acknowledge the key role played by courses like **Finite Element Methods, Theory of Elasticity, and Fracture Mechanics**, which provided the essential foundation for this work.

A heartfelt thanks to **my friends**, whose encouragement, patience, and company helped me stay motivated and positive throughout this academic journey.

Most importantly, I would like to thank **my parents and sister** for their unconditional love, continuous support, and belief in me. Their encouragement and sacrifices have been my greatest strength throughout every challenge.

Finally, thank you to everyone who contributed to this journey—your support has truly meant a lot. **Thank you, everyone**.

Devesh Agrawal

(M.Tech. in Mechanical Systems Design)

Dedicated to

My parents

Dileep Kumar Agrawal

&

Deepali Agrawal

Abstract

The objective of this thesis is to implement the spring element-based homogenization technique to perform periodic unit cell calculations within the ABAQUS finite element framework. Unit cell calculations are critical in the context of ductile failure analysis, as they provide a detailed understanding of localized deformation mechanisms, such as plastic flow and stress evolution.

A mathematical framework is implemented to represent the elastic–plastic behaviour of the matrix material, incorporating isotropic hardening under proportional loading conditions. The governing equations are formulated using finite strain theory and executed through finite element modelling using the ABAQUS/Standard implicit solver. The model utilizes spring elements to enforce periodic boundary conditions and control stress application, enabling simulations under controlled multiaxial stress states.

The results show that the accuracy of the unit cell simulation is primarily influenced by two key parameters: the spring stiffness and the size of the time increment. Improper calibration of these parameters can lead to notable deviations from target stress ratios, especially in the plastic regime. Through performance assessment and sensitivity analysis, the study identifies optimal ranges for these parameters, ensuring a balance between numerical accuracy and computational efficiency.

This work establishes a robust and adaptable approach to micromechanical simulation, with potential extensions to dynamic loading conditions and porous materials in future research.

TABLE OF CONTENTS

NOMENCLATURE

Symbols:

f	Porosity
σ	Microscopic Stress
$< \sigma >$	Macroscopic Stress
ρ	Ratio of Normal stresses
κ	Ratio of shear and Normal stress
F	Deformation Gradient
K	Spring Stiffness
ν	Poission's Ratio
E	Young's modulus
Ω	Volume of RVE
d^e	Elastic strain rate tensor
d^p	Plastic Strain rate Tensor
ε_0	Reference Plastic Strain

ACRONYMS

FEA	Finite Element Analysis
PBCs	Periodic Boundary Conditions
RVE	Representative Volume Element
MPC	Multi Point Constraints
UEL	User Defined Element
C3D8R	Continuum 3-Dimensional 8 noded linear brick element with reduced integration.
URDFIL	User Results Data File
UHARD	User-defined Hardening
GPa	Giga Pascal

LIST OF FIGURES

Chapter 1

Introduction

1.1 Overview: unit cell modeling

In computational mechanics, the need to understand material behaviour across different scales has led to the development of unit cell modelling. A unit cell, often referred to as a Representative Volume Element (RVE), is a small but statistically significant section of a material's microstructure. It serves as a bridge between microscopic features (like inclusions or voids) and the macroscopic properties observed in bulk materials.

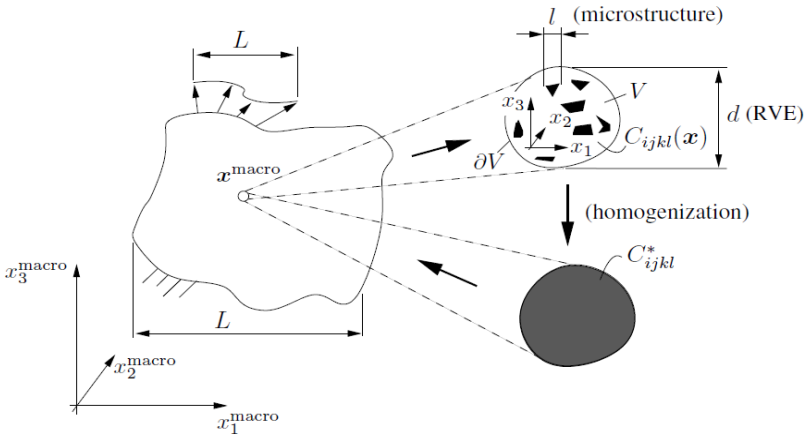

Fig.1.1 Homogenization and characteristic scales length (Gross and seelig, 2018)

The schematic above illustrates the concept of homogenization, where a microstructural volume with varying properties is mathematically averaged into an effective continuum representation

In this framework, the RVE (shown at the microscale) captures local heterogeneities, such as voids or grain boundaries, and the resulting data is used to derive homogenized material properties like effective stiffness C^*_{ijkl} . These properties are then applied at the macroscale to model the overall

material response without resolving every microstructural detail across the full structure.

To Perform unit cell calculation, Periodic Boundary Conditions (PBCs) are applied. These ensure that the displacements and tractions on opposite faces of the unit cell are matched, mimicking an infinite repetition of the microstructure. This approach avoids artificial edge effects and ensures consistent deformation behaviour across the cell.

By leveraging unit cell modelling and PBCs, researchers can perform high-fidelity micromechanical simulations while keeping computational costs manageable. This technique is widely used in materials science to evaluate how microstructural features influence bulk mechanical behaviour under complex loading scenarios.

1.2 Application in ductile failure analysis

Ductile failure in metals is a multiscale phenomenon typically governed by void nucleation, void growth, and void coalescence. These mechanisms evolve progressively under plastic deformation, leading to Plastic strain localization and eventual fracture. Understanding and predicting these events require detailed insight into how voids initiate and interact under various loading conditions.

Unit cell Simulation becomes essential in this context, as it allows direct simulation of individual voids embedded in a deforming matrix. By applying appropriate loading and boundary conditions to the unit cell, researchers can study the onset and evolution of void growth and coalescence and quantify their contribution to macroscopic failure. For example, analysing void growth under triaxial or shear loading helps determine critical conditions for damage initiation and fracture propagation.

Moreover, unit cell-based simulations provide a controlled platform to study how different factors—such as void shape, spacing, orientation, and

matrix hardening—affect the overall material response. These insights are crucial for developing and validating continuum-scale damage models used in large-scale structural simulations.

1.3 Thesis organization

This thesis is structured into seven chapters, each addressing a key component of the study:

Chapter 2: Literature review

The literature review focuses on existing algorithms for implementing periodic boundary conditions and proportional loading in unit cell simulations. Identification of research gap and problem statement.

Chapter 3: Homogenization technique

Overview of Technique used for performing unit cell calculations.

Chapter 4: Unit cell calculations

Description of the unit cell calculation in ABAQUS, including mesh, spring elements, and loading strategy.

Chapter 5: Results and discussion

Unit Cell calculation results, stress ratio accuracy, and effects of spring stiffness and increment size.

Chapter 6: Conclusions and future scope

Summary of key findings and future work on dynamic simulations and porous microstructures.

Chapter 2

Literature review and problem statement

2.1 Literature study

The progression of ductile failure in metallic materials typically follows three key stages: void nucleation, growth, and coalescence. As discussed in the work of Wiktor et al., (2016) voids generally form at microstructural features such as inclusions or second-phase particles where stress concentration occurs. As the material undergoes plastic deformation, these voids grows and begin to interact. Eventually, neighbouring voids link up in a process called coalescence, leading to the formation of localized band, where the plastic deformation starts accumulating, leading to final fracture.

Experimental studies have offered direct insight into this failure evolution. For example, Ravichandran et al., (2000). explored ductile fracture behaviour in high-strength steel under both quasi-static and dynamic loading conditions. Their findings highlighted how increased strain rates lead to more concentrated deformation zones, larger voids, and distinct shear-dominated fracture features. Through microscopy and thermal imaging, they identified phenomena such as void clustering, localized heating, and transition from uniform to tunnelled fracture surfaces. These results underscore the influence of loading rate and stress state on failure morphology.

To analyse such phenomena more systematically, researchers have turned to micromechanically motivated unit cell calculations. Most of these studies, disregards the void nucleation and assume a preexisting voids in the matrix. By using unit cell calculations, one can better understand how void

growth and localization contribute to macroscopic ductile failure, develop more accurate material models, and explore the effect of microstructural features on material performance.

These modelling efforts have led to the formulation of advanced constitutive models, such as the well-known Gurson (1977) model which incorporates void volume fraction into the yield criterion to capture damage accumulation and material softening.

In the context of unit cell calculations, several methods have been developed to maintain constant stress ratios during deformation, commonly referred to as proportional loading. In this study, we implement a spring-element-based approach that differs from the UEL-based formulation proposed by Chouksey et al., which utilizes auxiliary elements with displacement degrees of freedom to control generalized stress components. The UEL framework enables robust enforcement of multiaxial loading paths and facilitates stress-controlled deformation in periodic unit cells.

Additionally, the work by Vigneshwaran and Benzerga (2024), demonstrated an effective alternative approach, where spring elements were used to apply proportional loading in periodic unit cell simulations. This method simplifies the application of stress states while maintaining control over the deformation path, particularly in implicit solvers.

Building on these insights, the present study focuses on implementing a spring-element-based approach to perform unit cell calculations under proportional loading. The aim is to evaluate the performance of the algorithm in reproducing desired stress states and to assess how parameters such as spring stiffness and increment size influence accuracy and convergence.

2.2 Problem statement

This thesis focuses on Implementing a spring-based stress control technique, originally proposed by Vigneshwaran and Benzerga (2024), to simulate periodic unit cell behavior under proportional loading within the ABAQUS implicit framework. Although the method offers a simplified setup, its effectiveness in achieving target stress ratios, maintaining numerical stability, and responding to changes in key parameters like spring stiffness and increment size has not been systematically studied. This research aims to evaluate these aspects to establish reliable usage guidelines for unit cell calculations. Following are the key objectives

- Implement the spring-based stress control method within a periodic unit cell model using ABAQUS/Implicit.
- Validate the method's capability to maintain prescribed macroscopic stress ratios under proportional loading.
- Investigate the influence of spring stiffness and time increment size on stress accuracy and convergence.
- Determine optimal parameter ranges for achieving stable and accurate results.
- Provide a framework for extending the method to more complex loading and material conditions in future studies.

Chapter 3

Homogenization technique

3.1 Problem formulation

3.1.1Stress state dependencies

- **Macroscopic stress calculations**

The macro stress is defined as the volume average over the unit cell of the microscopic stress

$$< \sigma >= \frac{1}{\Omega}\int_{\Omega} \sigma d\Omega \quad (3.1)$$

Where Ω is volume of unit cell.

- **Stress triaxiality:** triaxiality is defined as the ratio of hydrostatic stress to equivalent (von Mises) stress.

$T = \frac{\sigma_m}{\sigma_{eq}}$, where (3.2)

$\sigma_{eq} = \sqrt{\frac{3}{2}\sigma' : \sigma'}$, $\sigma_m = \frac{<\sigma_1>+<\sigma_2>+<\sigma_3>}{3}$, $\sigma' = < \sigma > - \frac{1}{3} tr < \sigma >$.

- **Lode parameter:** It characterizes the effect of the third invariant of the deviatoric stress tensor and helps differentiate between stress states and is defined as:

$L = \frac{2<\sigma_2> - <\sigma_1> - <\sigma_3>}{<\sigma_3> - <\sigma_1>}$ (3.3)

Where $< \sigma_1 >, < \sigma_2 >, < \sigma_3 >$ are the principal stresses.

3.1.2 Deformation gradient tensor, F

The deformation gradient tensor, denoted by F, is a fundamental quantity in continuum mechanics used to describe how a material body deforms from

its original configuration to its current state. It captures both rigid body motion (rotation and translation) and local stretching or shearing of material elements. Mathematically, the deformation gradient is defined as

$$F = \frac{\partial x}{\partial X} \tag{3.4}$$

Where X is the position vector in the reference (undeformed) configuration and x is the position vector in the current (deformed) configuration.

3.1.3 Eulerian strain tensor, E

The Eulerian strain tensor, often referred to as the logarithmic strain tensor, is a strain measure used in finite deformation analysis. It is mathematically defined as

$E = \ln V$, where $V = FF^T$.Overall equivalent strain tensor is defined as

$$E_{eq} = \sqrt{\frac{2}{3}E' : E'}. \text{ Where } E' \text{ is deviatoric strain tensor.} \tag{3.5}$$

Unit cell in this study is subjected to one shear and three normal stress components. Hence, the non-zero components of E which can be derived from Wong and Guo, (2015) are as follows

$$E_{11} = \frac{1}{2}\ln(F_{11}F_{22}) + \frac{1}{2}\frac{{F_{12}}^2+{F_{11}}^2-{F_{22}}^2}{\gamma\delta}\ln\left(\frac{\gamma+\delta}{\gamma-\delta}\right), \tag{3.6}$$

$$E_{22} = \frac{1}{2}\ln(F_{11}F_{22}) + \frac{1}{2}\frac{{F_{12}}^2+{F_{11}}^2-{F_{22}}^2}{\gamma\delta}\ln\left(\frac{\gamma+\delta}{\gamma-\delta}\right), \tag{3.7}$$

$$E_{33} = \ln F_{33}, \tag{3.8}$$

$$E_{12} = \frac{F_{12}F_{22}}{\gamma\delta}\ln\left(\frac{\gamma+\delta}{\gamma-\delta}\right), \tag{3.9}$$

$$\text{where } \gamma = \sqrt{{F_{12}}^2 + (F_{12}+F_{22})^2},\ \delta = \sqrt{{F_{12}}^2 + (F_{12}+F_{22})^2}. \tag{3.10}$$

3.2 Implementation

3-D finite deformation calculations are carried out using the voided cell model. This framework was given by Vigneshwaran and Benzerga (2024). Initial dimension of unit cell is $2A_0$, $2A_0$, $2B_0$.

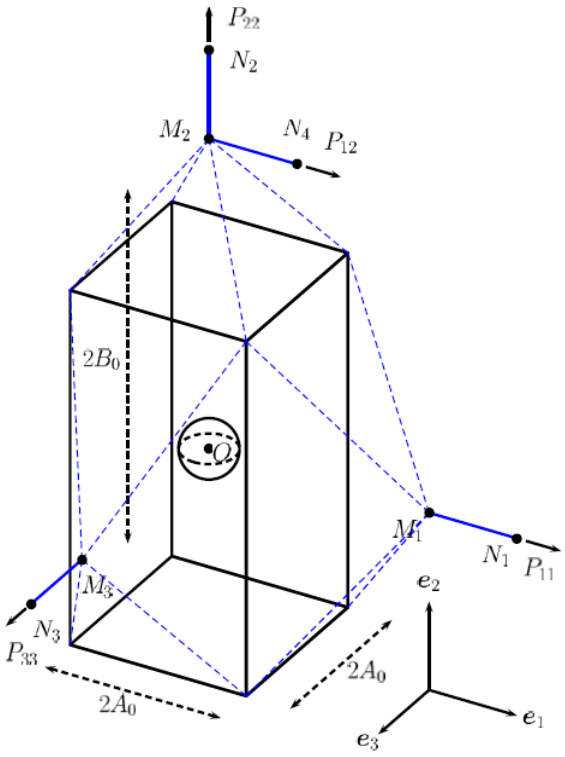

Fig. 3.1 Schematic of unit cell with master nodes and dummy nodes. Vigneshwaran and Benzerga (2024)

3.2.1 Boundary conditions

Fully periodic boundary conditions are applied on the unit cell. Relative displacements of points on opposite faces can be written as:

$$u(A_0, x_2, x_3) - u(-A_0, x_2, x_3) = 2A_0(F - I)e_1,$$

$$u(x_1, B_0, x_3) - u(x_1, -B_0, x_3) = 2B_0(F - I)e_2,$$

$$u(x_1, x_2, A_0) - u(x_1, x_2, -A_0) = 2A_0(F - I)e_3. \qquad (3.11)$$

Where F is the macro deformation gradient which is taken as the volume average of microscopic counterpart and x_i denotes coordinates in the initial configuration.

3.2.2 Loading condition

Proportional loading refers to a loading condition where the direction of the stress ratios remains constant.

In this study, proportional loading is characterized using two independent stress ratios, typically denoted as T and L. Proportional loading is considered using two stress ratios

$$\rho = \frac{\sigma_{11}}{\sigma_{22}} = \frac{\sigma_{33}}{\sigma_{22}}; \qquad \kappa = \frac{\sigma_{12}}{\sigma_{22}}. \tag{3.12}$$

Stress Triaxiality and Lode Parameter can be expressed in terms of these stress ratios given by Vigneshwaran and Benzerga (2024) as

$$T = \frac{(1+2\rho)\mathrm{sgn}\,(\sigma_{22})}{3\sqrt{(1-\rho)^2+3\kappa^2}}; \quad L = -\frac{(1-\rho)\mathrm{sgn}\,(\sigma_{22})}{\sqrt{(1-\rho)^2+4\kappa^2}}. \tag{3.13}$$

The periodic boundary condition has been imposed using the master nodes where the displacements of the master nodes are defined as

$$u^{M_1} = 2A_0(F-I)e_1,$$

$$u^{M_2} = 2B_0(F-I)e_2, \tag{3.14}$$

$$u^{M_3} = 2A_0(F-I)e_3.$$

By comparing eq. (3.14) with eq. (3.10) we get

$$u(A_0, x_2, x_3) - u(-A_0, x_2, x_3) = 2u^{M_1},$$

$$u(x_1, B_0, x_3) - u(x_1, -B_0, x_3) = 2u^{M_2}, \tag{3.14}$$

$$u(x_1, x_2, A_0) - u(x_1, x_2, -A_0) = 2u^{M_3}.$$

Macro deformation gradient is related to master nodes through

$$F=\begin{bmatrix} \frac{A}{A_0} & \frac{v}{B_0} & 0 \\ 0 & \frac{B}{B_0} & 0 \\ 0 & 0 & \frac{C}{A_0} \end{bmatrix}. \quad (3.15)$$

Where the current dimensions of the deformed unit cell can be calculated as $A = A_0 + u_1$, $A = A_0 + u_2$, $A = A_0 + u_3$ and ${u_1}^{M_1} = u_1$, ${u_2}^{M_2} = u_2$, ${u_3}^{M_3} = u_3$, ${u_1}^{M_2} = v$,The rate of deformation is then obtained as

$$D = \mathrm{Sym}(\dot{F}F^{-1}) = \begin{bmatrix} \frac{\dot{u_1}}{A} & \frac{1}{2}\left(\frac{\dot{v}}{B} - \frac{v\dot{u_1}}{AB}\right) & 0 \\ \frac{1}{2}\left(\frac{\dot{v}}{B} - \frac{v\dot{u_1}}{AB}\right) & \frac{\dot{u_2}}{B} & 0 \\ 0 & 0 & \frac{\dot{u_3}}{C} \end{bmatrix}. \quad (3.16)$$

Proportional stressing is applied by introducing nodal forces, which are related to the master displacement. If P_{ij} denotes the generalized force corresponding to degree of freedom i of master node j, the external power is

$$\dot{W}_{ext} = P_{11}\dot{u_1} + P_{22}\dot{u_2} + P_{33}\dot{u_3} + P_{12}\dot{v}. \quad (3.17)$$

The Hill–Mandel lemma is adopted to write the internal power of the cell as

$$\dot{W}_{int} = \Omega(\sigma_{11}D_{11} + \sigma_{22}D_{22} + \sigma_{11}D_{33} + 2\sigma_{12}D_{12}), \quad (3.18)$$

$$\dot{W}_{int} = \Omega\left[\left(\frac{\sigma_{11}}{A} - \frac{\sigma_{12}v}{AB}\right)\dot{u_1} + \left(\frac{\sigma_{22}}{B}\right)\dot{u_2} + \left(\frac{\sigma_{11}}{C}\right)\dot{u_3} + \left(\frac{\sigma_{12}}{B}\right)\dot{v}\right]. \quad (3.19)$$

Where Ω is volume of the unit cell, using the principle of virtual work, using eq. (3.17) and eq. (3.19) gives

$$P_{11} = \Omega\left(\frac{\sigma_{11}}{A} - \frac{\sigma_{12}v}{AB}\right), \qquad P_{22} = \Omega\left(\frac{\sigma_{22}}{B}\right),$$

$$P_{33} = \Omega\left(\frac{\sigma_{11}}{C}\right), \qquad P_{12} = \Omega\left(\frac{\sigma_{12}}{B}\right). \quad (3.20)$$

To achieve constant average stress ratios, direct application of forces to the master nodes is restricted by the constraint represented in Eq. (3.14). As a workaround, a penalty-based method is implemented where four spring elements are introduced to link the displacements of the master nodes with corresponding dummy nodes. Forces in springs are given by

$$P_{11} = \mathrm{k}(U_1 - u_1), \qquad P_{22} = k(U_2 - u_2),$$

$$P_{33} = \mathrm{k}(U_3 - u_3), \qquad P_{12} = \mathrm{k}(V - v). \tag{3.21}$$

Where k is stiffness of the spring. If the forces are normalized by a force P_{22}, following constraints are obtained.

$$U_1 - u_1 = \left(\frac{\rho B}{A} - \frac{\kappa v}{A}\right)(U_2 - u_2),$$

$$U_3 - u_3 = \left(\frac{\rho B}{C}\right)(U_2 - u_2), \tag{3.22}$$

$$V - v = \kappa(U_2 - u_2).$$

If the forces are normalized by a normal force P_{12}, following constraints are obtained

$$U_1 - u_1 = \left(\frac{\rho B}{\kappa A} - \frac{v}{A}\right)(V - v),$$

$$U_3 - u_3 = \left(\frac{\rho B}{\kappa C}\right)(V - v), \tag{3.23}$$

$$U_2 - u_2 = \frac{1}{\kappa}(V - v).$$

3.3 Displacement control strategy

The formulation involves solving a nonlinear system of equations that includes eight unknown displacements, $U_1, U_2, U_3, V, u_1, u_2, u_3, v$. These variables consist of four master nodes displacements and four dummy node displacements.

To enable numerical stability and ensure convergence, one of these displacement components is selected as a pilot or dummy variable. This

pilot displacement acts as a reference point for the iterative solution process, allowing the solver to anchor the system while calculating the remaining unknowns. As discussed by the Vigneshwaran and Benzerga (2024) choice of this control variable depends on the magnitude of the applied shear stress ratio, denoted as κ. When $\kappa < 0.7$, indicating that the loading is not predominantly shear-driven, the model utilizes Equation (3.27), assigning $U_2$the vertical displacement as the pilot. In cases where $\kappa > 0.7$, where shear dominates the loading scenario, Equation (3.28) is applied, and the tangential displacement V is used instead. This adaptive strategy ensures that the deformation applied to the unit cell closely mirrors realistic stress states, avoiding artificial constraints or instability in the numerical scheme.

This displacement control strategy is integral to the implementation of periodic boundary conditions, which simulate the effect of the unit cell being part of a larger, repeating structure. The control algorithm enables constant implementation of stress ratios in the unit cell, regardless of whether the dominant mode of loading is tension, compression, or shear. As a result, the model can accurately capture key micromechanical phenomena such as void elongation, rotation, and eventual coalescence, which are critical to predicting failure in porous and ductile materials.

Chapter 4

Unit cell calculations

4.1 Simulation setup and methodology

To numerically evaluate the mechanical response of the unit cell under multiaxial loading, a finite element model was developed using ABAQUS/CAE Standard 2017, as shown in Fig. 4.1. The unit cell was modeled with 27 eight-noded hexahedral elements (C3D8), and the discretization resulted in a total of 64 nodes.

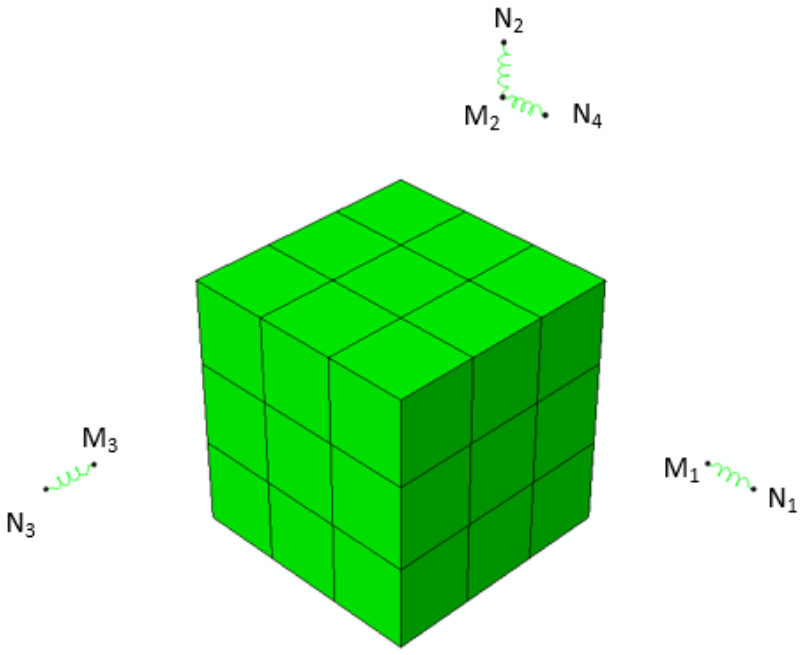

Fig. 4.1 Finite element mesh of the 3D unit cell with spring elements.

A structured hexahedral mesh was adopted due to its superior performance in capturing stress gradients compared to tetrahedral elements. Spring

elements were introduced along specific boundaries to simulate compliant loading and to control displacement transmission across the unit cell.

4.2 Boundary conditions and constraint implementation

To simulate the mechanical behaviour of the unit cell as part of a periodic microstructure, periodic boundary conditions (PBCs) were applied. These boundary conditions ensure that opposite faces of the unit cell deform in accordance with the displacement continuity condition (Eq. 3.11), enabling the model to represent the behaviour of an infinite, repeating material domain.

The displacement constraint in eq. 3.11 were implemented using the *Equation option available in ABAQUS. To streamline and automate this process, the Matlab scripting package, developed by Chouksey et al. (2019), was used. Matlab simplifies the generation of equation constraints across node sets on opposing faces, greatly reducing manual workload and improving accuracy in constraint application.

In addition to the periodic boundary condition, a user-defined multi-point constraint (MPC) subroutine was developed to control the stress ratios during the deformation. This subroutine adapts to the applied stress ratio (ρ & κ), eq. 3.12, switching between Equation (3.21) and Equation (3.22) to determine the appropriate control displacement using either the vertical component U_2 or the tangential displacement V as the pilot variable as suggested by Vigneshwaran and Benzerga (2024). This adaptive enforcement is critical for maintaining numerical stability, particularly under varied multiaxial loading conditions.

To monitor and record the material response throughout the simulation, the URDFIL subroutine was used to extract key output variables such as displacement of the master nodes at each increment. This procedure, in line with the methodology described by Chouksey et al., (2019), allows for

detailed analysis of evolving deformation patterns, void geometry, and porosity evolution.

Moreover, the implementation of the UHARD subroutine enabled the incorporation of a custom strain hardening law, allowing the model to update the material's yield stress in response to accumulated plastic strain. This subroutine plays a vital role in capturing the nonlinear material behaviour, ensuring that the hardening response is accurately reflected in the constitutive framework.

Collectively, these tools *Equation constraints, the MPC subroutine, and the URDFIL and UHARD routines provided a robust and flexible foundation for applying complex boundary conditions and tracking the micromechanical response of the unit cell under proportional loading conditions.

4.3 Spring stiffness and numerical stability

SPRINGA elements were used in ABAQUS to model compliant boundary loading conditions, allowing precise control over displacement application. Their implementation follows guidelines provided in the ABAQUS User Manual (2017) for spring-based interactions.

The use of spring elements in the finite element model plays a crucial role in stabilizing the simulation, particularly by controlling the pilot displacement and ensuring consistent deformation across the unit cell. Although the spring stiffness constant (k) does not appear directly in the normalized governing equations (Equations 3.27 and 3.28), its impact on iterative convergence is substantial. These springs are placed to facilitate smooth displacement transmission across boundaries while avoiding numerical instability.

In this study, a series of simulations were performed by varying the spring stiffness over a wide range—from 0.01 to 0.5 times of the value of E, where

E is the elastic modulus of the material. This range was selected to investigate the effect of spring stiffness on solution stability, convergence rate, and deformation accuracy. It was observed that very low stiffness value, 0.01 times the value of E, led to poor constraint control, while higher value, 0.5 times the value of E, introduced artificial stiffness that suppressed realistic deformation. Based on this analysis, a spring stiffness of approximately 0.1 times the value of E was found to provide optimal convergence and is adopted in simulations. Mesh refinement is necessary when inhomogeneities are present, as they cause local stress and strain variations that require a finer mesh for accurate results. The detailed influence of spring stiffness on simulation outcomes is presented in Chapter 5: Results and Discussion.

Chapter 5

Results and discussion

5.1 Constitutive behaviour of material

The mechanical response of the matrix is assumed to follow the rate independent isotropic J2 plasticity framework., where the elastic behavior has been defined with two elastic constants, modulus of elasticity, E=210GPa, and Poisson's ratio, ν=0.3.

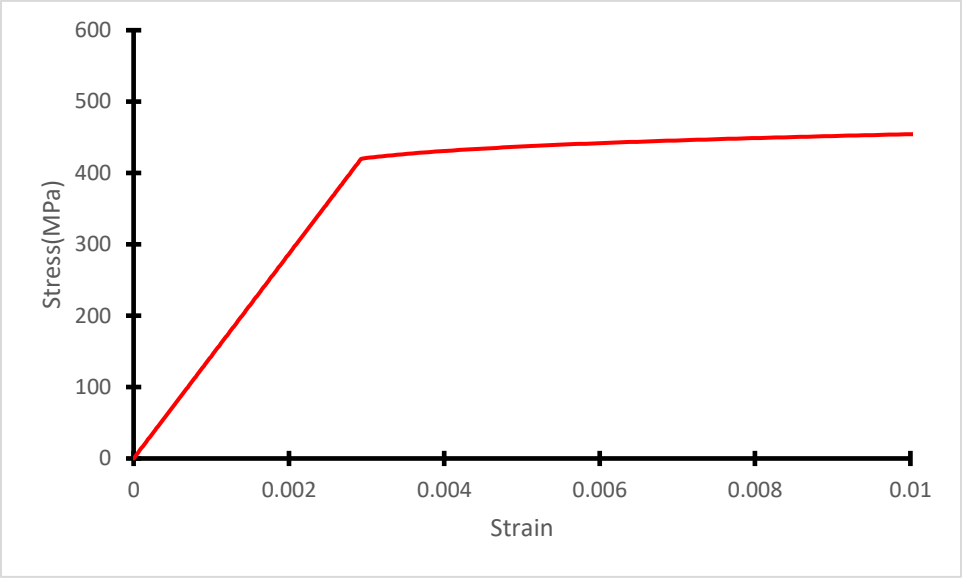

Fig 5.1 True stress versus True strain curve of material.

The power law isotropic hardening law has been considered as

$$\sigma_y = \sigma_0 \left(1 + \frac{\varepsilon}{\varepsilon_0}\right)^n \tag{5.1}$$

Here, σ_0 =420MPa represents the initial yield strength, ε_0 =0.002 is the reference plastic strain, and n=0.05, strain hardening exponent.

The stress-strain curve of the considered matrix material has been shown in Fig. 5.1. Since the unit cell contains no voids, the deformation response

remains homogeneous and primarily influenced by the intrinsic material properties rather than microstructural discontinuities.

5.2 Results

The results obtained from finite element unit cell calculations were analyzed based on the input stress ratios for two distinct loading conditions. Each case was evaluated, and any observed deviations are discussed in Section 5.3 under error analysis**.**

Case 1: ρ = 0.625, κ = 0

(Equivalent to T = 2, L = -1)

In this case, the loading corresponds to a triaxial stress state with no shear contribution. Since κ = 0, the shear component $< \sigma_{12} >$ is expected to be zero, eq. 3.12(b). In Fig. 5.2, stress field contours have been superimposed on the unit cell deformed configuration for different stresses at the same strain level. Contour plot shown in Fig. 5.2 (a) confirms this, showing negligible values of $< \sigma_{12} >$, thereby validating the absence of shear.

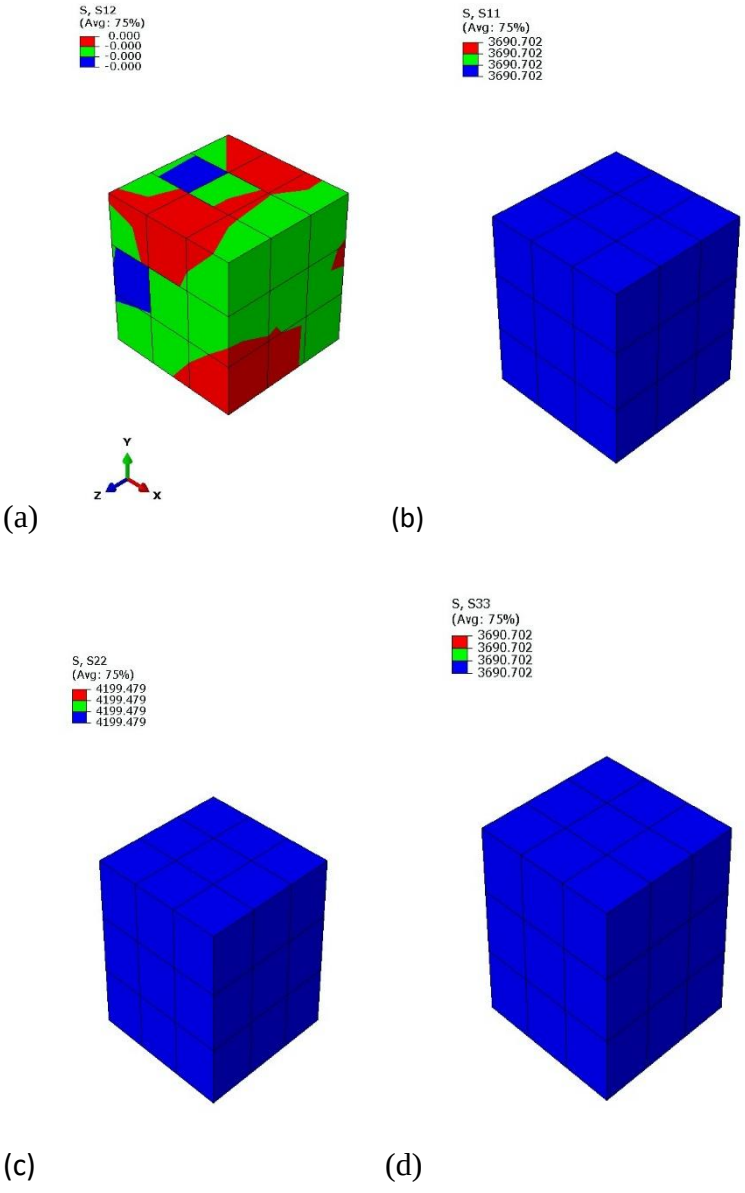

Fig. 5.2 The stress field contours have been superimposed on the unit cell deformed configuration for ρ = 0.625, and κ = 0 (a) $< \sigma_{12} >$, (b) $< \sigma_{11} >$, (c) $< \sigma_{22} >$ (d) $< \sigma_{33} >$.

The prescribed loading condition enforced equal axial stresses, $< \sigma_{11} > = < \sigma_{33} >$. The stress fields for $< \sigma_{11} >$ and $< \sigma_{33} >$ are near-identical, indicating axisymmetric deformation behavior with $< \sigma_{11} > = < \sigma_{33} >$.

The ratios $< \sigma_{11} > / < \sigma_{22} >$ and $< \sigma_{33} > / < \sigma_{22} >$ were prescribed to be equal and correspond to ρ = 0.625. While the output shows these ratios to be nearly identical, there is a slight deviation from the input values—this variation is attributed to numerical discretization and convergence tolerances, and is further discussed in Section 5.3.

Case 2: ρ = 1, κ = $\kappa = \frac{1}{\sqrt{3}}$

(Corresponding to T = 1, L = 0)

Second loading condition has been chosen with non-zero κ value. The chosen value of ρ = 1 and $\kappa = \frac{1}{\sqrt{3}}$ corresponds to, $< \sigma_{11} > = < \sigma_{22} > = < \sigma_{33} >$ along with $< \sigma_{12} > \neq 0$. In Fig. 5.3, stress field contours have been superimposed on the deformed configuration of the unit cell for different stresses corresponds to ρ = 1 and $\kappa = \frac{1}{\sqrt{3}}$. The contours show same normal stress level and $< \sigma_{12} >$ level corresponding to κ value.

Overall, the results from the second case also demonstrate that both the normal and shear stress components align well with input. The small variations observed in the output ratios are attributed to discretization and numerical approximations, which are further analyzed in Section 5.3.

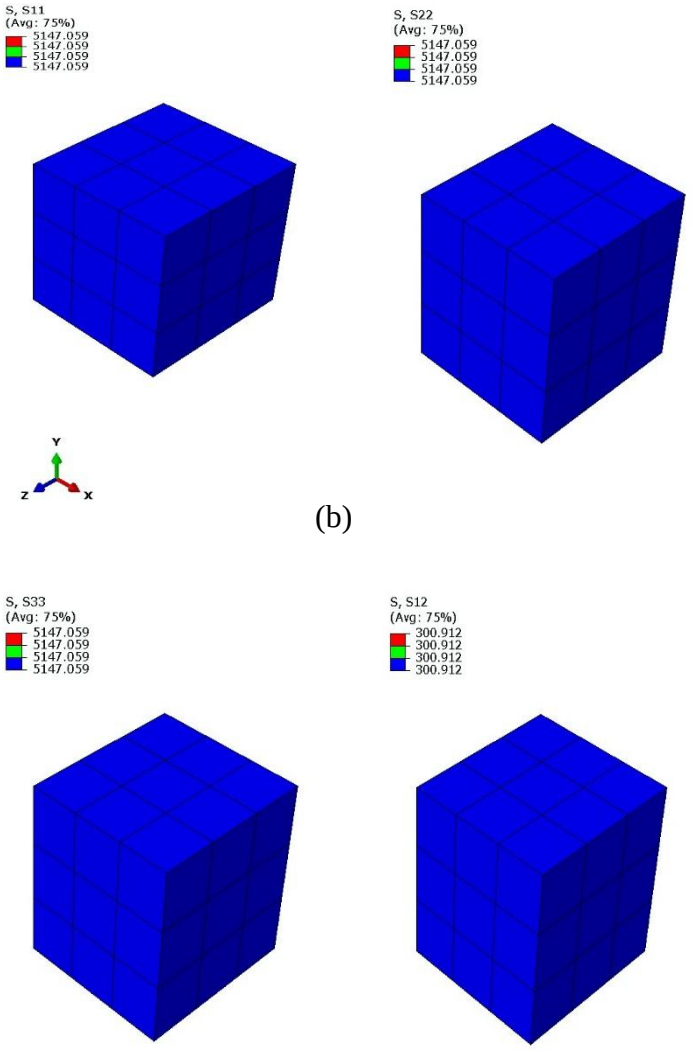

Fig. 5.3 The stress field contours have been superimposed on the unit cell deformed configuration for $\rho = 1$, $\kappa = \frac{1}{\sqrt{3}}$ (a) $< \sigma_{11} >$, (b) $< \sigma_{22} >$, (c) $< \sigma_{33} >$, (d) $< \sigma_{12} >$.

5.3 Algorithm calibration

The accuracy of the homogenization technique is evaluated by comparing the input stress ratios to the actual output stress ratios obtained from unit cell calculations. Deviations between these values are quantified as a percentage error and plotted against equivalent strain. It should be noted that since the void or inhomogeneity has not been considered in the unit

cell, there is no difference between micro and macro response of the unit cell. Two primary parameters influencing the performance are identified: spring stiffness (K) and finite element calculation increment size used during proportional loading.

5.3.1 Effect of time increment

Case: ρ = 0.625, κ = 0, K = 0.05E

In this case, simulations were performed with moderate spring stiffness (K =0.5 times the value of E) and constant increment size. The fig. 5.4 shows the percentage error in stress ratio as a function of equivalent strain. This setup helps evaluate the ability of the algorithm to maintain accurate stress ratio throughout both elastic and plastic loading regimes.

The plot shows that the error remains low during the elastic phase of loading, which indicates good stability and proper control of stress values at small strains. As the material transitions into the plastic regime, the error increases.

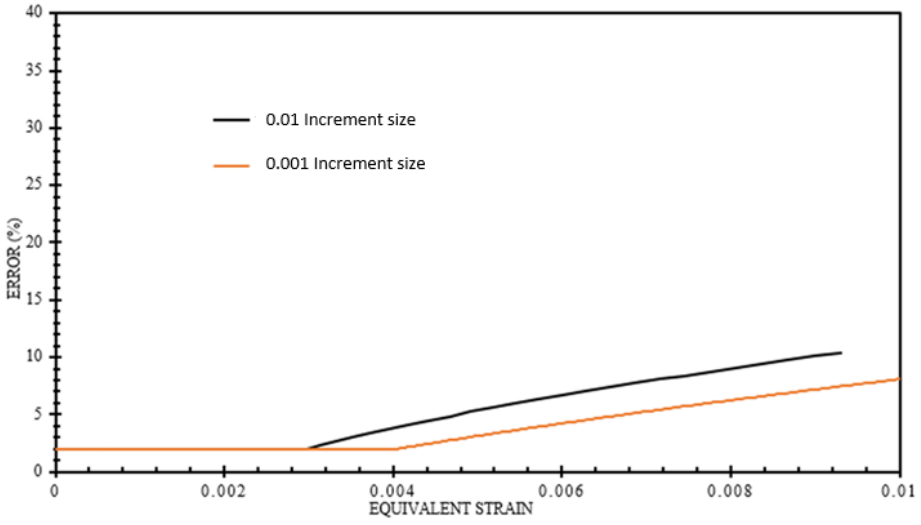

Fig. 5.4 Error (%) vs equivalent strain for K = 0.5 times the value of E

Further evaluation revealed that increasing the number of increments, in other words decreasing the time incitement improves stress control and reduces error. However, this improvement introduces a tradeoff: more increments significantly increase computational time, particularly in simulations involving complex or non-uniform material behaviour and finer meshes. After conducting several trials, it was found that smaller time increment, which is specific problem dependent provide a reasonable compromise between simulation accuracy and computational efficiency.

5.3.2 Effect of spring stiffness

Figure 5.5 shows the comparison between errors in stress ratio for different values of spring stiffness (0.5, 0.1, 0.05 and 0.01 times the value of E) as a function of equivalent strain. The errors have been plotted for proportional loading corresponding to $\rho = 0.625$, and $\kappa = 0$.

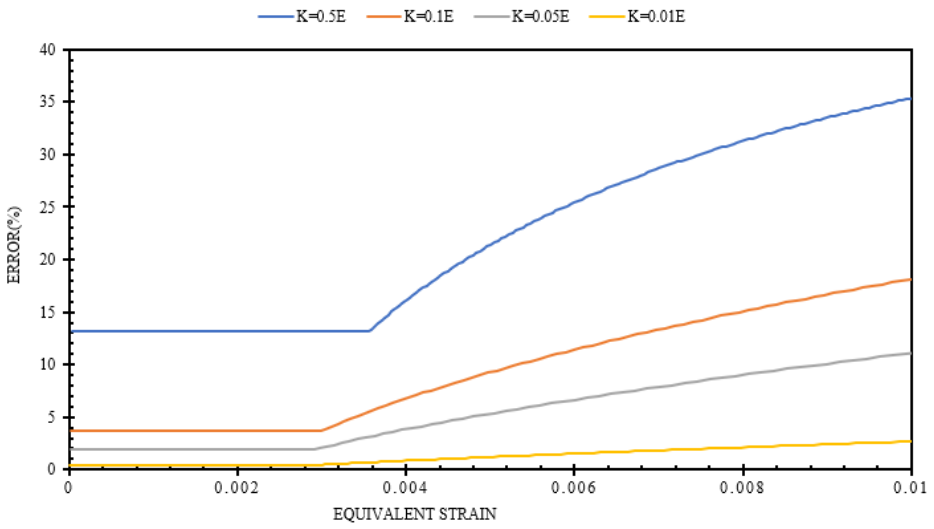

Fig. 5.5 Error (%) versus equivalent strain for different spring stiffness values, for proportional loading corresponding to $\rho = 0.625$, and $\kappa = 0$.

From the plot, it is evident that reducing the value of K leads to a noticeable decrease in error, particularly in the plastic deformation range. Among all cases, the lowest stiffness (K = 0.1 times the value of E) provides the best

accuracy, especially at higher strain levels where material behavior becomes increasingly nonlinear.

However, there is a computational tradeoff. For the same equivalent strain, smaller values of K require applying greater displacements and higher number of increments to reach the same strain level. This results in increased solver effort, more iterations, and higher computational time, especially when extended to complex models with refined meshes or inhomogeneous unit cell.

Therefore, while reducing K improves accuracy, it also increases the computational cost. A balance must be maintained, and the selection of K should consider both the required precision and available computational resources. Based on the trends observed, K = 0.05 times the value of E or 0.1 times the value of E may serve as a practical middle ground for most simulation setups.

Chapter 6

Conclusion and future scope

.6.1 Conclusion

In this study, a robust algorithm was successfully implemented the homogenization technique into the ABAQUS finite element framework to perform periodic unit cell calculations. The implementation allowed for accurate enforcement of periodic boundary conditions and flexible stress control through the use of custom subroutines and spring elements. A detailed performance assessment revealed that the accuracy of the algorithm is highly dependent on two critical parameters: spring stiffness and time increment size. Unit cell calculations showed that improper selection of these parameters leads to noticeable errors, especially in the plastic regime, while appropriate tuning significantly improves numerical stability and stress ratio accuracy.

To maintain this balance, each microstructural setup requires individual calibration to determine optimal stiffness and increment configurations. The results demonstrated for axisymmetric stress states. Furthermore, the methodology is not limited to symmetric conditions; it is readily extendable to general multiaxial loading scenarios, offering broad applicability in micromechanical studies of heterogeneous materials. Overall, the work establishes a practical and adaptable unit cell calculations framework that can support advanced material modelling and future investigations into complex microstructural behaviour.

6.2 Future scope

Building on the current work, future efforts are focused on developing a custom algorithm for periodic unit cell simulations under general loading conditions, including high strain rate scenarios, using the ABAQUS/Explicit framework. While the present study has been conducted using the implicit solver for quasi-static conditions, extending the methodology to explicit dynamics will allow for the simulation of complex, time-dependent material behaviour.

The upcoming implementation is specifically designed to model the dynamic response of porous materials under proportional and multiaxial loading, enabling detailed investigation into critical micromechanical phenomena such as void growth, interaction, and coalescence. These simulations will be further enhanced by considering variations in void geometry, spatial distribution, and porosity, offering a more comprehensive understanding of failure mechanisms at the microscale.

By integrating this capability into the explicit solver environment, the framework will be able to handle large deformations and high strain rate effects more efficiently, making it suitable for applications such as impact analysis, crash simulations, and dynamic fracture of ductile materials. This advancement will significantly broaden the applicability of the algorithm and contribute to predictive modelling of complex material behaviour under realistic service conditions.

References

[1] Wiktor Wcislik, Experimental determination of critical void volume fraction for the Gurson Tvergaard Needleman (GTN) model, Procedia Structural Integrity, Volume 2,2016.

[2] Venkert, A., Guduru, P.R. & Ravichandran, G. An investigation of dynamic failure in 2.3Ni-1.3Cr-0.17C steel. Metall Mater Trans A 31, 2000.

[3] Gurson, A.L. Continuum Theory of Ductile Rupture by Void Nucleation and Growth: Part 1—Yield Criteria and Flow Rules for Porous Ductile Media. Journal of Engineering Materials and Technology, 1977.

[4] Mayank Chouksey, Shyam M. Keralavarma, Sumit Basu, Computational investigation into the role of localisation on yield of a porous ductile solid, Journal of the Mechanics and Physics of Solids, 2019.

[5] Mayank Chouksey, Shyam M. Keralavarma, Sumit Basu, Exploring subtle features of yield surfaces of porous, ductile solids through unit cell simulations, Mechanics of Materials, 2020.

[6] Mayank Chouksey, Sumit Basu, Exploration of subsequent yield surfaces through unit cell simulation, International Journal of Solids and Structures, 2021.

[7] Mayank Chouksey, Shyam M. Keralavarma, Ductile failure under non-proportional loading, Journal of the Mechanics and Physics of Solids,2022.

[8] R. Vigneshwaran, A.A. Benzerga, An analysis of failure in shear versus tension, European Journal of Mechanics - A/Solids, 2024.

[9] R. Vigneshwaran, A.A. Benzerga, Assessment of a two-surface plasticity model for hexagonal materials, Journal of Magnesium and Alloys, 2023.

[10] W.H. Wong, T.F. Guo, On the energetics of tensile and shear void coalescences, Journal of the Mechanics and Physics of Solids, 2015.

[11] Dassault Systèmes, *ABAQUS 2017 Documentation*, Providence, RI: Simulia Corp., 2017

[12] Dietmar Gross, Thomas seelig, (2018) Fracture Mechanics with an introduction to micromechanics, Third Edition, Germany.